Eng. Sci., 2025, **35**, 1533

Engineered Science
DOI: https://dx.doi.org/10.30919/es1533

Dual Charge Transfer Channels over MXene into Zinc Indium Sulfide/Titanium Dioxide Composite Z-Scheme Heterostructure for Photocatalytic Benzyl Alcohol Oxidation Coupled with Hydrogen Production

Chao Cui,[1] Tao Yang,[1] Xiaolei Zhao,[3] Mingtao Li,[2] Xiaoning Wang,[4] Yuanhua Sang,[2,*] Hong Liu[2] and Jiahai Wang[1,*]

Abstract

Photocatalytic selective oxidation of alcohols to aldehydes coupled with H_2 production is an eco-friendly strategy for generating both high value-added chemicals and clean energy. In this study, a novel titanium carbide-zinc indium sulfide/titanium dioxide (Ti_3C_2-$ZnIn_2S_4/TiO_2$) heterostructure is assembled to photo-catalyze oxidation of benzyl alcohol (BA) into benzaldehyde (BAD) and coupled with H_2 production. The introduction of Ti_3C_2 as a potential regulator and the TiO_2 as the catalytic core of BA oxidation had a synergistic effect of H_2 and BAD production. Thus, the Ti_3C_2-ZIS/TiO_2 heterostructure exhibits an impressive BAD and H_2 production rate of 6.59 and 7.71 mmol g^{-1} h^{-1}, respectively. Additionally, this composite photocatalyst displays superior cyclic stability for simultaneous BA oxidation and H_2 production. The dual charge transfer channels constructed in the Ti_3C_2-ZIS/TiO_2 heterostructure have a crucial effect on enhancing the spatial separation and transport of carriers. This work supplies a promising strategy for constructing dual charge transfer channels to enhance the spatial isolation and gathering of charge carriers, aiming to achieve both high value-added chemical synthesis and clean H_2 energy production.

Keywords: MXene; $ZnIn_2S_4/TiO_2$; Z-scheme heterostructure; Benzyl alcohol oxidation; Hydrogen production.
Received: 27 March 2025; Revised: 01 May 2025; Accepted: 15 May 2025.
Article type: Research article.

1. Introduction

With the escalating environmental pollution and energy crisis, it is impressive to harness clean and renewable energy resources for the production of energy and chemicals. The significant step of selective aromatic alcohols oxidation to carbonyl compounds (e.g., acids, ketones, and aldehydes) is activating C-H bond.[1-4] These carbonyl products serve as crucial structural building blocks extensively utilized in pharmaceutical industries and fine chemicals.[5,6] Compared with traditional organic synthesis, which often requires harsh conditions, like high pressure or temperature, photocatalysis technology offers a promising approach to meet efficient synthetic reaction under mild conditions through the utilization of photogenerated charge carriers (electrons-holes) under excited states.[7-9] Among numerous research endeavors, photocatalytic aromatic alcohols oxidation typically occurs through utilizing molecular oxygen (O_2) as an oxidizing agent and electron acceptor. Reactive oxygen species, such as the singlet oxygen ($^1O_2$) and superoxide radical ($\cdot O_2^-$), have a beneficial effect of accelerating the oxidation rate of alcohols to carbonyl compounds.[10-13] Nevertheless, this aerobic method presents a drawback due to the wastage of photogenerated electrons in practical applications. Replacing oxygen with hydrogen protons for photo-redox reactions, especially in O_2-participated photocatalytic alcohol oxidation, makes full use of photogenerated charge carriers. In this point of view, photocatalytic oxidation of benzyl alcohol (BA) to benzaldehyde (BAD) coupled with hydrogen (H_2) production emerges as an eco-friendly strategy to simultaneously generate

---

[1] *School of Chemistry and Chemical Engineering, Guangzhou University, Guangzhou, 510000, China*
[2] *State Key Laboratory of Crystal Materials, Shandong University, Jinan, 250100, China*
[3] *School of Chemistry and Chemical Engineering, Taishan University, Taian, 271000, China*
[4] *School of Transportation and Civil Engineering, Shandong Jiaotong University, Jinan, 250357, China*
**E-mails*: sangyh@sdu.edu.cn (Y. Sang); jiahaiwang@gzhu.edu.cn (J. Wang)

clean energy fuel and high-value chemicals without introducing additional O_2 atmosphere and sacrificial agents.[14,15] However, the practical application of this promising strategy on a large scale is still restrained by challenges in photocatalysts,[16,17] such as weak light-harvesting capability, high recombination of photogenerated electrons and holes, and low charge utilization efficiency.

$ZnIn_2S_4$ (ZIS) has been applied as an efficient visible-light photocatalyst due to its suitable band structure.[18,19] However, pure ZIS often suffers from high recombination of photogenerated carriers and S^{2-} in ZIS undergoes photo-corrosion by holes, which inhibits its photocatalytic activity for redox reactions. To solve these problems, constructing Z-scheme heterostructures via energy band matching is an efficient strategy to improve the spatial separation and transport of charge carriers.[20-24] TiO_2, as an ultraviolet photocatalyst, has been widely used in BA oxidation with a commendable photocatalytic activity.[25,26] Thus, building ZIS/TiO_2 Z-scheme heterostructure is a feasible approach to simultaneous achieve BA oxidation and H_2 production without O_2 as electron trappers and extra sacrificial reagents. In order to further improve the carriers utilization efficiency and adjust the energy band structure, loading potential regulator on the surface of ZIS/TiO_2 heterostructure is an efficient strategy to achieve this aim. Ti_3C_2 as a kind of MXene materials, has attracted great attention in catalysis owing to its advantages of large specific surface area, excellent electronic conductivity, and abundant metal active sites.[27] The ternary heterostructure may possess dual interface electric filed to form dual charge transfer channels, which enhances the separation and transport of charge carriers directionally by the direction of electric filed. For example, Bai et al. reported a novel Ti_3C_2-$ZnIn_2S_4$-$NiSe_2$ heterojunction with multiple charge transfer channels for accelerated photocatalytic H_2 generation. The construction of Schottky junction between $ZnIn_2S_4$ and Ti_3C_2 could achieve the transport of the electrons from ZIS to Ti_3C_2 via the Schottky junction interface, while an internal electric field in S-scheme heterojunctions allows the migration of electrons from $NiSe_2$ to ZIS. To the best of our knowledge, it is rarely reported that integration Ti_3C_2 as potential regulator and electron mediator into ZIS/TiO_2 Z-scheme heterostructure with dual charge transfer channels to achieve efficient BA oxidation and H_2 production, simultaneously.

In this work, a novel MXene Ti_3C_2-ZIS/TiO_2 heterostructure has been developed to modulate catalytic activity for simultaneous BA oxidation coupled with H_2 production. Dual charge transfer channels are constructed in the ternary Ti_3C_2-ZIS/TiO_2 heterostructure to have a synergistic effect of enhancing the separation and transport of photocatalytic carriers. The Z-scheme heterostructure between ZIS and TiO_2 is constructed in the Ti_3C_2-ZIS/TiO_2 composite materials. The electrons produced by TiO_2 are recombinant with the holes produced by ZIS, leaving the holes produced by TiO_2 to achieve efficient BA oxidation. On the other hand, the electrons are transferred from ZIS to Ti_3C_2 for the reduction of proton (H^+) to H_2. The Ti_3C_2 as a potential regulator and the TiO_2 as the catalytic core of BA oxidation have a synergistic effect of efficient H_2 (7.71 mmol g^{-1} h^{-1}) and BAD production (6.59 mmol g^{-1} h^{-1}). Besides, this ternary heterostructure exhibited superior photocatalytic activity compared to other reported photocatalysts for the same purpose.

2. Experimental

2.1 Materials

Thioacetamide (CH_3CSNH_2, 99%), zinc acetate ($Zn(OAc)_2{\cdot}2H_2O$, 99%), and indium trichloride tetrahydrate ($InCl_3{\cdot}4H_2O$, 99%) were obtained from Sinopharm Chemical Reagent Co., Ltd. (Shanghai, China). Titanium dioxide (TiO_2, P25) was purchased from Degusse Co., Ltd. (Germany). Titanium carbide (Ti_3C_2, 99%) was purchased from Mingchang new material Technology Co., Ltd. (Nanjing, China). Ultrapure water from UPHW-III-90T system was used to prepare the solutions.

2.2 Synthesis of ZIS

For the synthesis of ZIS, $InCl_3{\cdot}4H_2O$ (146.6 mg, 0.5 mmol), $Zn(OAc)_2{\cdot}2H_2O$ (54.9 mg, 0.25 mmol) and CH_3CSNH_2 (112.7 mg, 1.5 mmol) were successively dissolved in deionized water (50 mL). The solution was transferred to a Teflon-lined autoclave (100 mL) at 180 °C for 3 h. Subsequently, the yellow precipitate was obtained by centrifugation at 8000 rpm·min^{-1} for 5 min and washed with deionized water and ethanol for three times in sequence. The yellow powder was dried under vacuum at 60 °C for 12 h.

2.3 Synthesis of the ZIS/TiO_2 and Ti_3C_2-ZIS heterostructure

TiO_2 powder (30 mg) was uniformly dispersed in deionized water (50 mL) by sonication and stirring for 30 min in sequence. The multilayer Ti_3C_2 (5 mg) was added to deionized water (50 mL) and sonicated for 2 h to peel into fewer layers, respectively. The next step is same for the synthesis of ZIS. Then, $InCl_3{\cdot}4H_2O$ (146.6 mg, 0.5 mmol), $Zn(OAc)_2{\cdot}2H_2O$ (54.9 mg, 0.25 mmol) and CH_3CSNH_2 (112.7 mg, 1.5 mmol) were added to the suspension and dissolved in water by stirring for 30 min. The mixed system was transferred to a Teflon-lined autoclave (100 mL) at 180 ºC for 3 h. Subsequently, the precipitate was obtained by centrifugation at 8000 rpm·min^{-1} for 6 min and washed with deionized water and ethanol for three times in sequence. The powder was dried under vacuum at 60 °C for 12 h. The mass ratio of TiO_2 to ZIS was 30% for the ZIS/TiO_2 heterostructure. The mass ratio of Ti_3C_2 to ZIS was 5% for the Ti_3C_2-ZIS heterostructure, respectively.

2.4 Synthesis of the Ti_3C_2-ZIS/TiO_2 heterostructure

The different weight of multilayer Ti_3C_2 (1, 3, 5, 7 and 10 mg) was added to deionized water (50 mL) and sonicated for 2 h to peel into fewer layers, respectively. TiO_2 powder (30 mg) was added, sonicated and stirred for 30 min in sequence to form a uniformly dispersed suspension. Then, $InCl_3{\cdot}4H_2O$ (146.6 mg, 0.5 mmol), $Zn(OAc)_2{\cdot}2H_2O$ (54.9 mg, 0.25 mmol) and

CH_3CSNH_2 (112.7 mg, 1.5 mmol) were added to the above suspension and dissolved in deionized water by sonication and stirring. The mixed system was transferred to a Teflon-lined autoclave (100 mL) at 180 ºC for 3 h. After reaction, the precipitate was obtained by centrifugation at 10000 rpm·min^{-1} for 10 min and washed with deionized water and ethanol for three times in sequence. The powder was dried under vacuum at 60 °C for 12 h. The mass ratio of Ti_3C_2 to ZIS in the Ti_3C_2-ZIS/TiO_2 heterostructure was 1, 3, 5, 7 and 10%, respectively. The mass ratio of TiO_2 to ZIS was fixed at 30% for the various Ti_3C_2-ZIS/TiO_2 heterostructure. The fixed mass ratio of TiO_2 to ZIS was aimed at explore the influence of Ti_3C_2 content to the photocatalytic activity in the various Ti_3C_2-ZIS/TiO_2 heterostructure.

2.5 Photoelectrochemical tests

The photoelectrochemical tests were performed using a traditional three-electrode system at a CHI660E potentiostats. The Ag/AgCl (saturated KCl aqueous solution) electrode and the Pt sheet electrode were used as the reference electrode and counter electrode, respectively. The preparation of the working electrode was listed as follows: polyvinylidene fluoroacetic acid (60 μL) and 1-methyl-2-pyrrolidinone (50 μL) were added to the photocatalyst powder (10 mg) and grounded evenly in sequence. It was then evenly brushed on the upper surface of F-doped SnO_2 (FTO) conductive glass, and finally vacuum dried at 60 ºC for 12 h. The transient photocurrent response was recorded at 50 s intervals under light on and off with a bias voltage of 0.1 V. Xenon lamp (300 W) was used as the light source and an aqueous solution of Na_2SO_4 (pH = 7, 0.5 M) was used as the electrolyte, respectively. Electrochemical impedance spectroscopy (EIS) measurements were measured at open-circuit voltages with a frequency range of 0.01 to 100 kHz at an amplitude of 50 mV.

2.6 Photocatalytic benzyl alcohol oxidation and occupied with hydrogen production test

The photocatalytic selective oxidation of benzyl alcohol occupied with hydrogen production was performed in a custom quartz glass reactor (100 mL). First, the photocatalyst (30 mg) was dispersed in deionized water (50 mL) by sonication and stirring for 30 minutes in sequence to form a uniformly dispersed suspension. Benzyl alcohol (1 mL, 1 mmol) was then added and dissolved in water by stirring for 30 min. Xenon lamp (300 W) was used as the light source to irradiate the reactor vertically. Before light illumination, the reaction system was under vacuum to remove the oxygen. The system was stirred under dark for 30 min to reach the adsorption equilibrium. Then, the system was reacted for 4 h under light illumination and kept at 10 ºC by condensing circulating water. When the reaction finished, the suspension was passed through a 0.22 μm aqueous membrane filter to remove the photocatalyst. The solution was injected into a liquid chromatograph (C18 column, injection volume: 20 μL, water : methanol = 30 : 70, detection wavelength: 254 nm, flow rate: 1.0 mL·min^{-1}, column temperature: 30 ºC) to quantify the concentration of benzyl alcohol and benzaldehyde after the reaction.

3. Results and discussion

3.1 Characterization of the Ti_3C_2-ZIS/TiO_2 heterostructure

The Ti_3C_2-ZIS/TiO_2 heterostructure was prepared via in-situ growing ZIS on the surface of uniformly dispersed Ti_3C_2 sheets with decoration of TiO_2 on ZIS's surface (Fig. 1a). X-ray diffraction (XRD) was applied to analyze the crystal structures of the photocatalysts (Fig. 1b). The XRD pattern (Fig. S1) of individual Ti_3C_2 was consistent with its crystal planes. The XRD pattern of pure ZIS could be indexed to a hexagonal $ZnIn_2S_4$ phase (JCPDS No. 65–2023).[28] TiO_2 showed its diffraction peaks that could be assigned to the anatase (JCPDS No. 65–0190) and rutile (JCPDS No. 65–5714) composite phases.[29] The 5% Ti_3C_2-ZIS/TiO_2 heterostructure exhibited the characteristic peaks of both hexagonal $ZnIn_2S_4$ and TiO_2 phases. However, due to the high dispersion and low loading of Ti_3C_2 in the ZIS/TiO_2 heterostructure, the 5% Ti_3C_2-ZIS/TiO_2 heterostructure did not showed obvious diffraction peaks of Ti_3C_2.[30] The Raman spectra further confirmed the existence of Ti−C bond in Ti_3C_2 at 159 cm^{-1}, this bond was also observed in the Ti_3C_2-ZIS/TiO_2 heterostructure (Fig. 1c). The above results demonstrated the successful synthesis of the Ti_3C_2-ZIS/TiO_2 heterostructure. Besides, the Zeta potentials of ZIS and TiO_2 were measured to be −17.9 and 15.2 mV, respectively (Figs. 1d and S2). This suggests that ZIS and TiO_2 were equipped with negative and positive charges, respectively. Thus, TiO_2 nanoparticles could be easily adsorbed on the surface of ZIS via electrostatic interaction. The Zeta potentials of the ZIS/TiO_2 heterostructure was measured to be −13.7 mV via interaction by TiO_2 and ZIS.

Scanning and transmission electron microscopies (SEM, TEM) were applied to characterize the morphology structure of the photocatalysts. Before exfoliation, the Ti_3C_2 powder exhibited a multilayered structure (Fig. S3a). After exfoliation, it transformed into a single or few-layered structure with a length of several microns. ZIS exhibited a nanoflower structure composed of numerous nanosheets, each was several hundred nanometers in length (Fig. S3b). TiO_2 appeared as spheroidal nanoparticles with a nanoscale size of ~25 nm (Fig. S3c). The SEM image of Ti_3C_2-ZIS heterostructure revealed intertwined sheets of Ti_3C_2 and ZIS (Figs. S4a and S4b). The morphology of the ZIS/TiO_2 heterostructure featured small nanoparticles on the surface of a nanoflower assembled from multiple nanosheets (Figs. S4c and S4d). The Ti_3C_2-ZIS/TiO_2 heterostructure revealed TiO_2 nanoparticles dispersed on the surface of ZIS nanosheets, with Ti_3C_2 sheets tightly bound to ZIS nanoflowers by SEM image (Fig. 1e). The TEM image exhibited an interlacing arrangement of Ti_3C_2, ZIS, and TiO_2 (Fig. S5). Additionally, the high resolution TEM (HR-TEM) image of the Ti_3C_2-ZIS/TiO_2 heterostructure showed the lattice fringes with 0.35, 0.32, and 0.26 nm d-spacings, corresponding to TiO_2's (0110) crystal facet,[27] ZIS's (102)

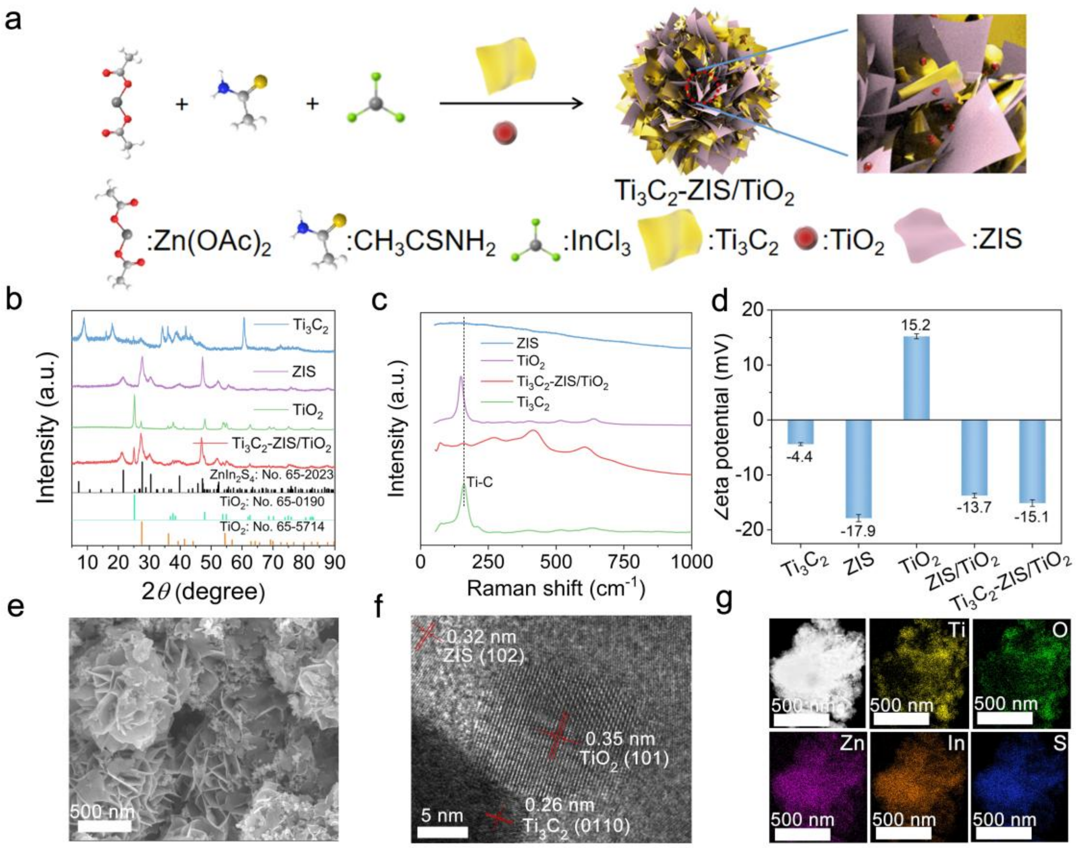

Fig. 1: (a) Schematic diagram for the synthesis of the Ti_3C_2-ZIS/TiO_2 heterostructure; (b) XRD patterns of Ti_3C_2, TiO_2, ZIS, and the 5% Ti_3C_2-ZIS/TiO_2 heterostructure; (c) Raman spectra of Ti_3C_2 and the Ti_3C_2-ZIS/TiO_2 heterostructure; (d) Zeta potentials of Ti_3C_2, ZIS, TiO_2, ZIS/TiO_2, and the Ti_3C_2-ZIS/TiO_2 heterostructure; (e) SEM images; (f) HR-TEM image and (g) EDX mapping images of the Ti_3C_2-ZIS/TiO_2 heterostructure.

crystal facet,[31] and Ti_3C_2's (101) crystal facet,[32] respectively (Fig. 1f). The Ti_3C_2-ZIS/TiO_2 heterostructure showed a uniform distribution of Zn, Ti, S, In, and O elements by energy dispersive X-ray spectroscopy (EDX) mapping images (Fig. 1g).

3.2 Photocatalytic performance analysis of the ZIS/TiO_2 heterostructure for simultaneous BA oxidation and H_2 production

The photocatalytic performance of BA oxidation coupled with H_2 production of the catalysts was evaluated in an aqueous solution under full spectrum irradiation without addition of extra sacrificial agents. The H_2 production curves within a 4 h reaction period displayed a steady increase in the H_2 amount (Fig. S6). Then, the BAD and H_2 production rate of the photocatalysts were calculated and compared (Fig. 2a). The individual TiO_2 showed inferior BAD and H_2 production rates as low as 0.03 mmol g^{-1} h^{-1}, attributed to the severe recombination of photogenerated carriers. The individual ZIS exhibited relatively higher rates of 1.32 mmol g^{-1} h^{-1} for H_2 production. When ZIS and TiO_2 constructed heterostructure, the BAD and H_2 production rates of the ZIS/TiO_2 heterostructure reached to 2.86 and 3.36 mmol g^{-1} h^{-1}, which were 2.55 and 95.33 times greater than those of ZIS and TiO_2 alone, respectively. Thus, the construction of ZIS/TiO_2 heterostructure supplies electron transfer channel betweeen TiO_2 and ZIS to enhance the transport of charge carriers.

3.3 The optical and photoelectrochemical performance of the ZIS/TiO_2 heterostructure

Furthermore, the surface elemental states and chemical compositions of the photocatalysts were analyze by the X-ray photoelectron spectroscopy (XPS). The survey scan of ZIS/TiO_2 revealed signals of Ti, Zn, O, S, and In elements (Fig. S7). In the Ti 2p XPS spectrum of TiO_2, the peaks at 464.12 and 458.39 eV were assigned to Ti $2p_{1/2}$ and $2p_{3/2}$ doublets,[25] respectively (Fig. 2b). For the ZIS/TiO_2 heterostructure, the corresponding peaks were shifted to 464.38 and 458.79 eV towards higher binding energies (BEs) compared to pure TiO_2. In the O 1s XPS spectrum of TiO_2, the deconvoluted peaks at 529.61 and 531.41 eV were assigned to the Ti-O and OH bonds, respectively (Fig. 2c). In the ZIS/TiO_2 heterostructure, the corresponding bonds were blue-shifted to 531.79 and 530.03 eV, respectively. The peaks located at 1022.34 and 1045.45 eV were assigned to Zn $2p_{3/2}$ and $2p_{1/2}$ doublets of ZIS (Fig. 2d).[26] As for the ZIS/TiO_2 heterostructure, these two doublets were red-shifted to 1045.06 and 1022.09 eV, respectively. The corresponding peaks at 452.44 and 444.91 eV were attributed to In $3d_{3/2}$ and $3d_{5/2}$ doublets of ZIS, respectively (Fig. 2e). Notably, these two doublets in ZIS/TiO_2

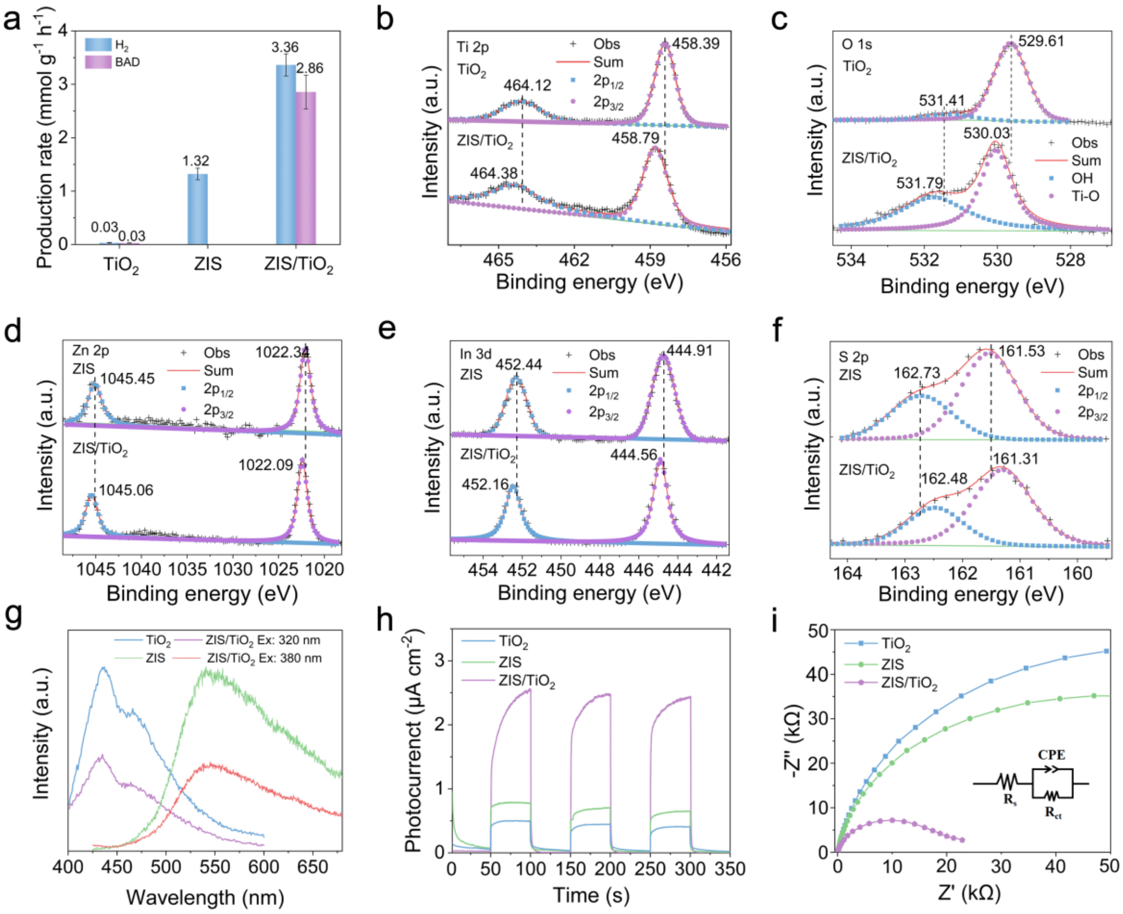

Fig. 2: (a) Photocatalytic BA oxidation coupled with H_2 production rate of TiO_2, ZIS and the ZIS/TiO_2 heterostructure; (b) Ti 2p and (c) O 1s XPS spectra of TiO_2 and the ZIS/TiO_2 heterostructure; (d) Zn 2p, (e) In 3d, and (f) S 2p XPS spectra of ZIS and the ZIS/TiO_2 heterostructure; (g) The PL spectra of TiO_2, ZIS and ZIS/TiO_2 heterostructure excited at 320 and 380 nm; (h) Transient photocurrent response and (i) Nyquist plots of TiO_2, ZIS, the ZIS/TiO_2 heterostructure.

were red-shifted to 452.16 and 444.56 eV compared with pure ZIS. Furthermore, the deconvoluted peaks at 162.73 and 161.53 eV can be corresponding to S $2p_{1/2}$ and $2p_{3/2}$ doublets of ZIS, respectively (Fig. 2f). As for the ZIS/TiO_2 heterostructure, these peaks were shifted to 152.48 and 161.31 eV, respectively. According to the above results, the peaks of Ti and O elements in the ZIS/TiO_2 heterostructure were all shifted towards higher BEs compared to pure TiO_2, indicating that TiO_2 lost electrons. Meanwhile, the peaks of S, In, and Zn elements in the ZIS/TiO_2 heterostructure were all shifted towards lower BEs compared to pure ZIS, suggesting that ZIS accepted electrons. In conclusion, the electrons were shifted from TiO_2 to ZIS in the ZIS/TiO_2 heterostructure. The opposite shifts in BEs for TiO_2 and ZIS after building the ZIS/TiO_2 heterostructure. The opposite shifts in BEs for TiO_2 and ZIS after building the ZIS/TiO_2 heterostructure would be tightly linked to the electric field between TiO_2 and ZIS. An electron transfer channel could be constructed directed from TiO_2 to ZIS in the ZIS/TiO_2 heterostructure.

The light absorption capabilities of TiO_2, ZIS, and the ZIS/TiO_2 heterostructure was evaluated by the Ultraviolet–visible diffuse reflectance spectra (UV-vis DRS). TiO_2 showed a response to ultraviolet light (Fig. S8), while ZIS demonstrated extended absorption from ultraviolet to visible light range. When combined into a heterostructure, ZIS/TiO_2 showed comparable ultraviolet to visible light absorption compared to individua ZIS. The steady-state solid photoluminescence (PL) spectra demonstrated that pure ZIS displayed a strong fluorescence emission peak at 542 nm under an excitation wavelength of 380 nm (Fig. 2g). The fluorescence intensity of ZIS/TiO_2 heterostructure was 51% lower than that of pure ZIS, attributable to the charge transfer channel at the interface of ZIS/TiO_2 heterostructure. The fluorescence intensity of the Ti_3C_2-ZIS/TiO_2 heterostructure was an additional 37% lower compared to the ZIS/TiO_2 heterostructure, due to the construction of a ternary heterostructure that enhances charge separation. Similarly, pure TiO_2 exhibited an emission peak at 435 nm under an excitation wavelength of 320 nm. The fluorescence intensity of ZIS/TiO_2 heterostructure was 46% lower than that of pure TiO_2, attributed to the formation of a binary heterostructure that effectively suppressed charge carriers recombination.

Besides, the fluorescence intensity of Ti_3C_2-ZIS/TiO_2 heterostructure was 28% lower than that of the ZIS/TiO_2 heterostructure, indicating that the ternary heterostructure further enhanced the charge carriers separation and transport. Additionally, the photoelectrochemical performance of the catalysts was evaluated using transient photocurrent response and electrochemical impedance spectra (EIS) measurements. The photocurrent densities of TiO_2 and ZIS were 0.5 and 0.8 μA cm^{-2}, respectively (Fig. 2h). However, when Ti_3C_2 and ZIS formed a Schottky barrier, the Ti_3C_2-ZIS heterostructure showed the photocurrent density to 1.5 μA cm^{-2}, showing a 1.9-fold increase than that of pure ZIS, highlighting the important role of heterostructure in enhancing charge separation through charge transfer channel. Furthermore, the ZIS/TiO_2 heterostructure reached to 2.2 μA cm^{-2}, its photocurrent density was 4.4 and 2.8 times higher than that of TiO_2 and ZIS, respectively. This increasement indicated that construction of heterostructure effectively promoted the electron transport. Notably, the Ti_3C_2-ZIS/TiO_2 heterostructure exhibited the highest photocurrent density of 3.0 μA cm^{-2} among the investigated photocatalysts, indicating a synergistic enhancement in electron transport due to the formation of dual internal electric fields. Moreover, EIS measurements demonstrated that the Ti_3C_2-ZIS/TiO_2 heterostructure showed the smallest resistance value than that of TiO_2, ZIS, Ti_3C_2-ZIS, and ZIS/TiO_2 heterostructure (Fig. 2i), indicating that the Ti_3C_2-ZIS/TiO_2 heterostructure is beneficial to promote efficient separation and transfer of photogenerated electrons and holes among Ti_3C_2, ZIS and TiO_2 components, thereby minimizing interfacial transfer resistance through the creation of dual electron transfer channels.

3.4 Band structure analysis of the ZIS/TiO_2 heterostructure

The energy band structures of ZIS and TiO_2 were analyzed using UV-vis DRS and Mott-Schottky curves. The band gap energies (E_g) of TiO_2 and ZIS were found to be 3.31 and 2.46 eV, respectively (Fig. 3a). Meanwhile, the conduction band (CB) values of TiO_2 and ZIS were determined from the Mott-Schottky curves as –0.46 and –0.19 V versus normal hydrogen electrode (vs. NHE), respectively (Figs. 3b and 3c). Thus, the valance band (VB) values of ZIS and TiO_2 were calculated as 2.00 and 3.12 V (vs. NHE), respectively. Furthermore, the electron paramagnetic resonance (EPR) spectra were applied through 5, 5-dimethyl-1-pyrroline-N-oxide (DMPO) as a spin trapping reagent to detect hydroxyl radical (•OH) and superoxide radical (•O_2^-). The literature data reported that the standard potential of OH^-/•OH was referenced as 2.38 V (vs. NHE).[30] As shown in Fig. 3d, pure TiO_2 showed a DMPO-•OH quartet signal with an intensity ratio of 1:2:2:1 under light irradiation. In contrast, pure ZIS did not produce •OH signal under light irradiation. The ZIS/TiO_2 heterostructure displayed a stronger •OH signal compared to pure TiO_2, which was 3.0 fold compared to TiO_2 alone, revealing that the building of ZIS/TiO_2 heterostructure could produce more isolated holes to form radical •OH. Besides, the literature reported the standard potential of O_2/•O_2^- to be −0.33 V (vs. NHE).[33-35]

Pure TiO_2 could produce weak •O_2^- signal with an intensity ratio of 1:1:1:1 under light irradiation (Fig. 3e), while ZIS exhibited a stronger •O_2^- signal than TiO_2. The ZIS/TiO_2 heterostructure could produce the highest •O_2^- signal among TiO_2, ZIS and ZIS/TiO_2. The signal intensity of the •O_2^- for ZIS/TiO_2 heterostructure was 8.87 and 4.36-fold compared to that of pure TiO_2 and ZIS, respectively. If TiO_2 and ZIS formed type II heterostructure, the photogenerated electrons would transfer from the CB of ZIS to the CB of TiO_2 (Fig. S9). The photogenerated holes would transfer from the VB of TiO_2 to the VB of ZIS. However, the VB of ZIS (2 V) was lower than the standard potential of OH^-/•OH (2.38 V), while the CB of ZIS (−0.19 V) was higher than the standard potential of O_2/•O_2^- (−0.33 V). Theoretically, this arrangement would not lead to the formation of the •OH and •O_2^- signal in the ZIS/TiO_2 heterostructure. However, this theoretical expectation contradicted the findings from the EPR analysis. Thus, the ZIS/TiO_2 heterostructure cannot be classified as a type II heterostructure. If considering the construction of a Z-scheme heterostructure between TiO_2 and ZIS, electrons were predicted to transfer from the CB of TiO_2 to combine with the photogenerated holes at the VB of ZIS (Fig. 3f). In this configuration, the CB of ZIS (−0.46 V) was lower than the standard potential of O_2/•O_2^- (−0.33 V), and the VB of TiO_2 (3.12 V) was higher than the standard potential of OH^-/•OH (2.38 V). As a result, the •OH and •O_2^- signal of the ZIS/TiO_2 heterostructure could indeed be produced. This prediction is consistent with the EPR result, affirming the successful formation of a Z-scheme heterostructure in the ZIS/TiO_2 system. The TiO_2 in the ZIS/TiO_2 heterostructure is the core of catalytic oxidation of BA to BAD.

3.5 Photocatalytic performance analysis of the Ti_3C_2-ZIS/TiO_2 heterostructure for simultaneous BA oxidation and H_2 production

In order to further enhance the carriers utilization rate of the photocatalysts, Ti_3C_2 was coupled into the photocatalysts system. The photocatalytic performance of the photocatalysts with different Ti_3C_2 content was evaluated by BA oxidation coupled with H_2 production. As shown in Fig. 4a, the H_2 production curves within a 4 h reaction period displayed a steady increase in the H_2 amount. When 5% Ti_3C_2 and TiO_2 formed Schottky junction, the photocatalytic H_2 and BAD production rates of 5% Ti_3C_2-TiO_2 were 2.00 and 1.67 times higher than that of pure TiO_2. When 5% Ti_3C_2 and ZIS formed Schottky junction, the photocatalytic H_2 production rate of 5% Ti_3C_2-ZIS was 2.42 mmol g^{-1} h^{-1}, respectively, which was 1.83 times higher than that of pure ZIS. When the mass ratio of Ti_3C_2 to ZIS reached 1%, this ternary 1% Ti_3C_2-ZIS/TiO_2 heterostructure demonstrated superior H_2 and BAD production rates of 4.86 and 4.29 mmol g^{-1} h^{-1}, respectively (Fig. 4b). When the mass ratio of Ti_3C_2 to ZIS reached 3%, the H_2 and BAD production rates of 3% Ti_3C_2-ZIS/TiO_2 heterostructure were 5.44 and 4.98 mmol g^{-1} h^{-1}, respectively.

When increasing the mass ratio of Ti_3C_2/ZIS to 5%, the Ti_3C_2-ZIS/TiO_2 heterostructure achieved the optimized H_2 and BAD production rates of 7.71 and 6.59 mmol g^{-1} h^{-1}, approximately 2.29 and 2.30 times higher than those of ZIS/TiO_2, respectively. Notably, the H_2 and BAD production rates of the 5% Ti_3C_2-ZIS/TiO_2 heterostructure were 5.84 and

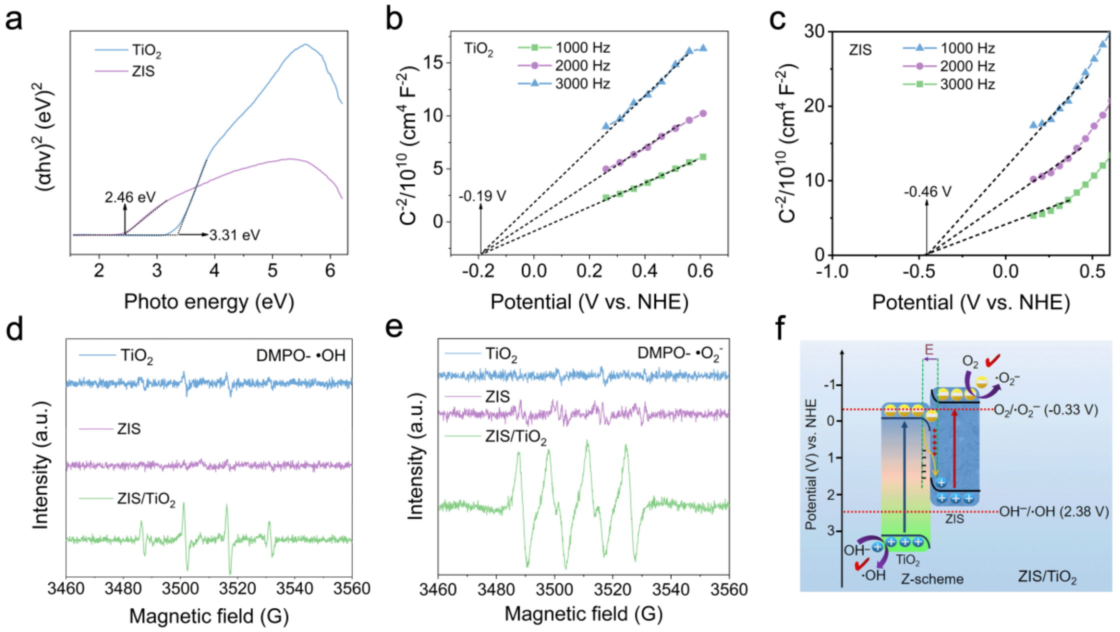

Fig. 3: (a) Transformed Kubelka-Munk function plots for TiO_2 and ZIS; (b-c) The Mott-Schottky curves of (b) TiO_2 and (c) ZIS; (d-e) DMPO spin-trapping (d) •OH radical and (e) •O_2^- radical EPR analysis for TiO_2, ZIS, and the ZIS/TiO_2 heterostructure under light irradiation; (f) The schematic diagrams of the ZIS/TiO_2 heterostructure for Z-scheme mechanism.

5.83 times higher than those of pure ZIS, respectively. The introduction of Ti_3C_2 in the ZIS/TiO_2 heterostructure served as potential regulator and electron mediator to enhance the separation and utilization of electrons for H_2 production. However, the H_2 and BAD production rates of 7% Ti_3C_2-ZIS/TiO_2 heterostructure were reduced to 6.92 and 6.51 mmol g^{-1} h^{-1} compared to that of the 5% Ti_3C_2-ZIS/TiO_2 heterostructure, respectively. The 10% Ti_3C_2-ZIS/TiO_2 heterostructure exhibited decreased production rates (6.12 and 5.53 mmol g^{-1} h^{-1} for H_2 and BAD production) compared to the 7% Ti_3C_2-ZIS/TiO_2 heterostructure. This decrease could be attributed to the excessive Ti_3C_2 content hindering the light absorption of ZIS/TiO_2 (Fig. S10). Notably, the photocatalytic performance of the 5% Ti_3C_2-ZIS/TiO_2 heterostructure also exhibited superiority when compared with the photocatalysts reported in recent literatures for the same purpose (Fig. 4c and Table S1).

Additionally, cycling tests were conducted to evaluate the stability of the Ti_3C_2-ZIS/TiO_2 heterostructure in the BA oxidation and H_2 production. Notably, the 5% Ti_3C_2-ZIS/TiO_2 heterostructure displayed steady linear curves of H_2 production over four cyclic tests (Fig. 4d), with photocatalytic BAD and H_2 production rates remained above 91.3% and 93.7%, respectively, after four reaction cycles (16 h) (Fig. 4e). The post-mortem XRD pattern of Ti_3C_2-ZIS/TiO_2 after four reaction cycles was consistent with that before reaction (Fig. S11), indicating the exceptional structural durability of the Ti_3C_2-ZIS/TiO_2 heterostructure. Furthermore, the influence of light intensity and reaction temperature to the photocatalytic performance of the Ti_3C_2-ZIS/TiO_2 heterostructure was explored. As shown in Fig. S12a, the photocatalytic performance of Ti_3C_2-ZIS/TiO_2 heterostructure was basically proportional to the light intensity. The photocatalytic H_2 production rates were 2.42, 5.32 and 7.71 mmol g^{-1} h^{-1} at the low, middle and high light intensity (50, 100 and 150 mW cm^{-2}), respectively. Meanwhile, the photocatalytic BAD production rates were 2.02, 4.65 and 6.59 mmol g^{-1} h^{-1} at the low, middle and high light intensity (50, 100 and 150 mW), respectively. Besides, the photocatalytic activity of Ti_3C_2-ZIS/TiO_2 heterostructure was gradually enhanced with the increase of reaction temperature (Fig. S12b). The photocatalytic H_2 production rates were 6.82, 7.71, 8.23 and 8.58 mmol g^{-1} h^{-1} at the temperature of 5, 10, 15 and 20 °C, respectively. Meanwhile, the photocatalytic BAD production rates were 6.15, 6.59, 7.22 and 7.82 mmol g^{-1} h^{-1} at the temperature of 5, 10, 15 and 20 °C, respectively.

In order to explore the active species for BA oxidation over the Ti_3C_2-ZIS/TiO_2 heterostructure, different trapping agents were applied to control experiments. Specifically, tetrachloromethane (CCl_4), isopropanol (IPA) and triethanolamine (TEOA) were selected as scavengers for trapping electrons (e$^-$), hydroxyl radicals (•OH) and holes (h$^+$), respectively. The Ti_3C_2-ZIS/TiO_2 heterostructure with the addition of CCl_4 demonstrated superior BAD production rate of 7.28 mmol g^{-1} h^{-1}, which enhanced 12.3% compared with the same photocatalyst without CCl_4. The introduction of CCl_4 consumed more electrons generated by the Ti_3C_2-ZIS/TiO_2 heterostructure, leaving more available holes to take part in the oxidation of BA. The BAD production rate of the Ti_3C_2-ZIS/TiO_2 heterostructure in the presence of IPA was reduced 30.1% compared to that without IPA, the generation of •OH consumed a part of holes that led to the reduction of BAD production rate. Besides, The BAD production rate of the Ti_3C_2-ZIS/TiO_2 heterostructure in the presence of TEOA was reduced 62.7% compared to that without IPA, suggesting that holes played an important role in the conversion of BA to BAD.

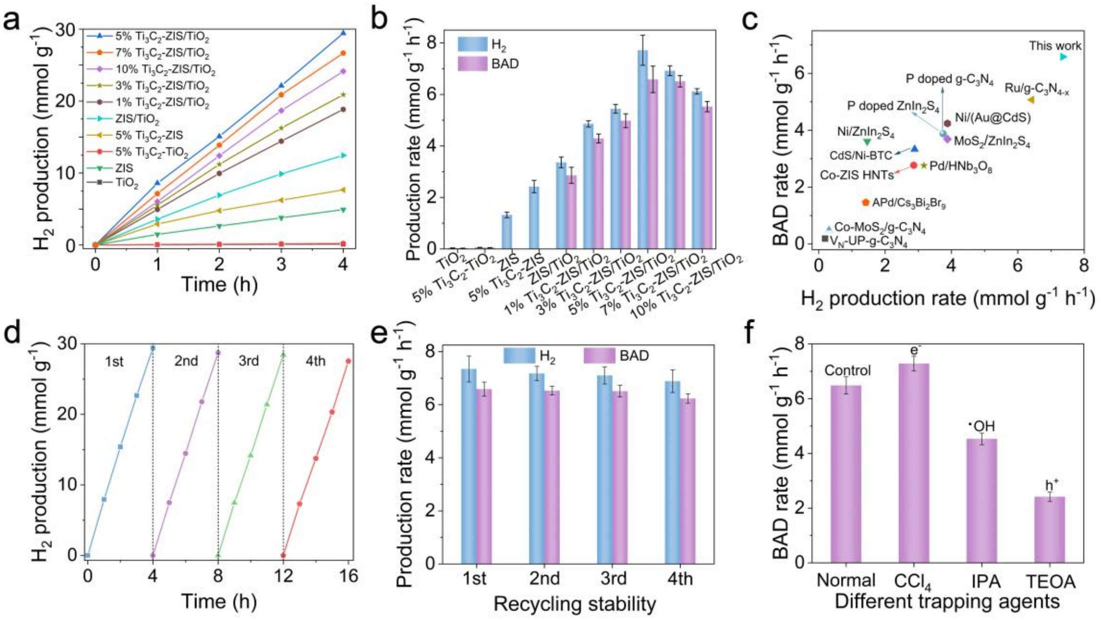

Fig. 4: (a) Time-dependent H_2 production of different photocatalyst; (b) Photocatalytic BAD and H_2 production rate of different photocatalysts; (c) The photocatalytic performance comparison of 5% Ti_3C_2-ZIS/TiO_2 with reported works for the same purpose; (d) Cycling stability of 5% Ti_3C_2-ZIS/TiO_2 for H_2 production; (e) Production rates of BAD and H_2 over the 5% Ti_3C_2-ZIS/TiO_2 photocatalyst during four cycles; (f) Photocatalytic BAD production rate in controlled experiments using different trapping agents on BA oxidation over the Ti_3C_2-ZIS/TiO_2 heterostructure.

Besides, the apparent quantum efficiency (AQE) of Ti_3C_2-ZIS/TiO_2 for BA oxidation coupled with H_2 production was measured to be 0.35% under 400 nm monochromatic irradiation (Fig. S13). The above results collectively demonstrated the excellent photocatalytic activity and reaction stability of Ti_3C_2-ZIS/TiO_2 for realizing efficient BA oxidation coupled with H_2 production.

3.6 The XPS analysis, optical and photoelectrochemical performance of the Ti_3C_2-ZIS/TiO_2 heterostructure

The surface elemental states and chemical compositions of the ZIS/TiO_2 and Ti_3C_2-ZIS/TiO_2 heterostructure were analyze by the XPS. The survey scan of ZIS/TiO_2 revealed signals of Ti, Zn, O, S, and In elements (Fig. S14), aligning with the findings of EDX spot analysis (Fig. S15). The peaks located at 1045.06 and 1022.09 eV were assigned to Zn $2p_{1/2}$ and $2p_{3/2}$ doublets of the ZIS/TiO_2 heterostructure (Fig. 5a). As for the Ti_3C_2-ZIS/TiO_2 heterostructure, these two doublets were shifted to 1045.15 and 1022.15 eV, respectively. The corresponding peaks at 452.16 and 444.56 eV were attributed to In $3d_{3/2}$ and $3d_{5/2}$ doublets of the ZIS/TiO_2 heterostructure, respectively (Fig. 5b). Notably, these two doublets in the Ti_3C_2-ZIS/TiO_2 heterostructure were shifted to 452.32 and 444.72 eV compared with the ZIS/TiO_2 heterostructure. Furthermore, the deconvoluted peaks at 162.48 and 161.31 eV can be corresponding to S $2p_{1/2}$ and $2p_{3/2}$ doublets of the ZIS/TiO_2 heterostructure, respectively (Fig. 5c). As for the ZIS/TiO_2 heterostructure, these peaks were shifted to 162.55 and 161.35 eV, respectively. In conclusion, the electrons were shifted from ZIS to Ti_3C_2 in the Ti_3C_2-ZIS/TiO_2 heterostructure for protons reduction to produce H_2.

Besides, the steady-state solid PL spectra demonstrated that the fluorescence intensity of the Ti_3C_2-ZIS/TiO_2 heterostructure excited at 380 nm was an additional 37% lower compared to the ZIS/TiO_2 heterostructure (Fig. 5d), due to the construction of a ternary heterostructure that enhanced charge transfer between Ti_3C_2 and ZIS/TiO_2. Similarly, the fluorescence intensity of Ti_3C_2-ZIS/TiO_2 heterostructure excited at 320 nm was 28% lower than that of the ZIS/TiO_2 heterostructure (Fig. 5e), indicating that the ternary heterostructure further enhanced the charge carriers separation and transport. Additionally, the photoelectrochemical performance of the ZIS/TiO_2 and Ti_3C_2-ZIS/TiO_2 heterostructure was evaluated using transient photocurrent response and EIS measurements. Notably, the Ti_3C_2-ZIS/TiO_2 heterostructure exhibited the photocurrent density of 3.0 μA cm^{-2} (Fig. 5f), which was 1.4 times higher than that of the ZIS/TiO_2 heterostructure. This increasement indicated that construction of ternary Ti_3C_2-ZIS/TiO_2 heterostructure effectively promoted the electron transport. Moreover, EIS measurements demonstrated that the Ti_3C_2-ZIS/TiO_2 heterostructure showed lower resistance value than that of the ZIS/TiO_2 heterostructure (Fig. 5g), indicating that the Ti_3C_2-ZIS/TiO_2 heterostructure was beneficial to promote efficient separation and transfer of photogenerated charge between Ti_3C_2 and ZIS/TiO_2, thereby minimizing interfacial transfer resistance through the creation of dual interfacial electron fields.

3.7 Band structure and the reaction mechanism of the Ti_3C_2-ZIS/TiO_2 heterostructure for simultaneous BA oxidation coupled with H_2 production

Based on the aforementioned results, the Ti_3C_2-ZIS/TiO_2 heterostructure achieved efficient BA oxidation and H_2

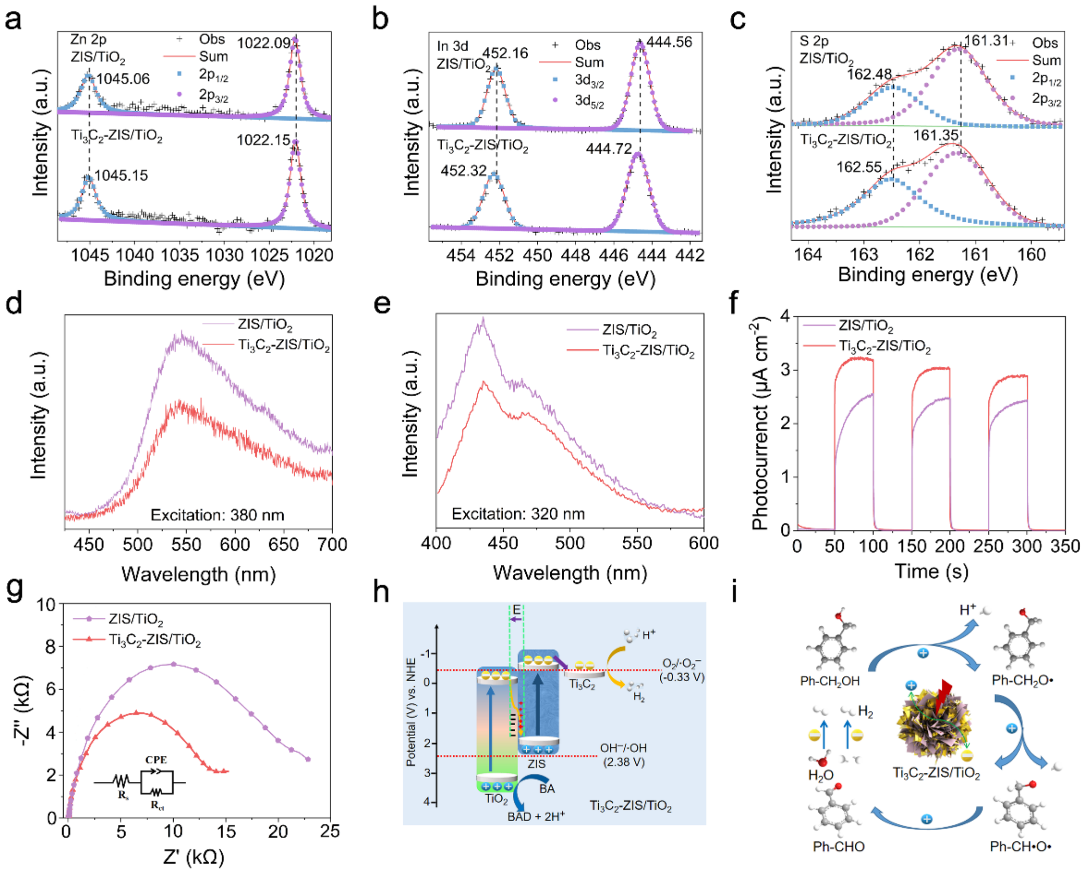

Fig. 5: (a) Zn 2p, (b) In 3d, and (c) S 2p XPS spectra of the ZIS/TiO_2 and Ti_3C_2-ZIS/TiO_2 heterostructure; The PL spectra of the ZIS/TiO_2 and Ti_3C_2-ZIS/TiO_2 heterostructure excited at (d) 380 nm and (e) 320 nm, respectively; (f) Transient photocurrent response and (g) Nyquist plots of the ZIS/TiO_2 and Ti_3C_2-ZIS/TiO_2 heterostructure; (h) Energy band structure schematic diagram and (i) the reaction mechanism of the Ti_3C_2-ZIS/TiO_2 heterostructure for simultaneous BA oxidation coupled with H_2 production.

production simultaneously. The proposed mechanism is illustrated in Figs. 5h and 5i. Under light irradiation, ZIS and TiO_2 in the Ti_3C_2-ZIS/TiO_2 heterostructure were photoexcited, generating electrons and holes. Electrons were transferred from the CB of TiO_2 and paired with the photogenerated holes at the VB of ZIS through an electron transfer channel. An internal electric field was established between ZIS and TiO_2 in the Ti_3C_2-ZIS/TiO_2 heterostructure, directed from ZIS to TiO_2. The leaving holes at the VB of TiO_2 participated in the oxidation of BA. Initially, one BA molecule was absorbed on the surface of the Ti_3C_2-ZIS/TiO_2 heterostructure. Subsequently, a hydrogen proton was abstracted from the OH group of BA by a hole, leading to its adsorption on the photocatalyst surface, leaving behind an alkoxide anion (Ph-CH_2O^-). Another hole attacked and cleaved the C_α-H bond in Ph-CH_2O^-, producing a carbon-centered radical (Ph-CH•O•), with the resulting proton also adsorbed on the photocatalyst surface. Finally, a hole located at the surface of TiO_2 continued to oxidize Ph-CH•O•, yielding BAD product. The TiO_2 in the Ti_3C_2-ZIS/TiO_2 heterostructure was the core of catalytic oxidation of BA to BAD. Hydrogen protons for this process originated from both BA oxidation and H_2O splitting. The Fermi Energy (E_f) level of Ti_3C_2 was −0.1 V (vs. NHE).[36] The potential of Ti_3C_2 was closer to 0 V compared with ZIS, thus, Ti_3C_2 was easier to produce H_2 compared with ZIS. Meanwhile, electrons generated at the CB of ZIS were transferred to the surface of Ti_3C_2 through an electron transfer channel, facilitating efficient proton reduction to produce H_2. Besides, the Ti_3C_2 nanosheets in the Ti_3C_2-ZIS/TiO_2 heterostructure may serve as an electron mediator to promote the transport of electrons between $ZnIn_2S_4$ and TiO_2.

4. Conclusion

In summary, a bifunctional Ti_3C_2-ZIS/TiO_2 heterostructure was demonstrated to achieve high-value BAD production and clean H_2 energy generation. The dual charge transfer channels constructed by the Ti_3C_2-ZIS/TiO_2 heterostructure significantly enhanced the spatial separation and transport of cariers. The introduction of Ti_3C_2 in the Ti_3C_2-ZIS/TiO_2 heterostructure could serve as a potential regulator and electron mediator to enhance electron transport and H_2 production. As a result, the Ti_3C_2-ZIS/TiO_2 heterostructure exhibited efficient BAD (6.59 mmol g^{-1} h^{-1}) and H_2 production rate (7.71 mmol g^{-1} h^{-1}), respectively. Additionally, the Ti_3C_2-ZIS/TiO_2 heterostructure displayed superior photocatalytic activity compared to other reported photocatalysts for the same purpose. Furthermore, it showed high stability in reaction and cyclic performance during BA oxidation coupled with H_2 production. This work supplies a promising strategy for the design of Z-scheme heterostructure with dual charge transfer channels to enhance the spatial isolation and gathering of charge carriers, aiming to achieve both high value-added chemical synthesis and clean H_2 energy production.

Acknowledgements

The authors acknowledge funding supports from the National Natural Science Foundation of China (Grant Nos. 52102278, 22074025), the Natural Science Foundation of Shandong Province (No. ZR2021ME207), and Guangzhou Municipal Science and Technology Project (No. 2024A03J0087).

Conflict of Interest

There is no conflict of interest.

Supporting Information

Applicable.

References

[1] M. Y. Qi, M. Conte, M. Anpo, Z. R. Tang, Y. J. Xu, Cooperative coupling of oxidative organic synthesis and hydrogen production over semiconductor-based photocatalysts, *Chemical Reviews*, 2021, **121**, 13051-13085, doi: 10.1021/acs.chemrev.1c00197.

[2] J. Z. Zhen, J. H. Sun, X. W. Xu, Z. L. Wu, W. K. Song, Y. Z. Ying, S. K. Liang, L. S. Miao, J. Z. Cao, W. Y. Lv, C. S. Song, Y. Y. Yao, M. Y. Xing, M-N_3 configuration on boron nitride boosts singlet oxygengeneration via peroxymonosulfate activation for selective oxidation, *Angewandte Chemie International Edition*, 2024, **63**, e202402669, doi: 10.1002/anie.202402669.

[3] W. Li, Y. M. Mao, Z. L. Liu, J. S. Zhang, J. H. Luo, L. Zhang, Z. A. Qiao, Chelated ion-exchange strategy toward biocl mesoporous single-crystalline nanosheets for boosting photocatalytic selective aromatic alcohols oxidation, *Advance Materials*, 2023, **35**, 2300396, doi: 10.1002/adma.202300396.

[4] Y. L. Liu, Y. N. Zheng, D. Y. Feng, L. L. Zhang, L. Zhang, X. W. Song, Z. A. Qiao, Efficient selective oxidation of aromatic alkanes by double cobalt active sites over oxygen vacancy-rich mesoporous Co_3O_4, *Angewandte Chemie International Edition*, 2023, **62**, e202306261, doi: 10.1002/anie.202306261.

[5] D. Y. Tang, G. L. Lu, Z. W. Shen, Y. Z. Hu, L. Yao, B. F. Li, G. X. Zhao, B. X. Peng, X. B. Huang, A review on photo-, electro- and photoelectro- catalytic strategies for selective oxidation of alcohols, *Journal of Energy Chemistry*, 2023, **77**, 80-118, doi: 10.1016/j.jechem.2022.10.038.

[6] F. L. Liu, X. T. Gao, R. Shi, Z. X. Guo, E. C. M. Tse, Y. Chen, Concerted and selective electrooxidation of polyethyleneterephthalate-derived alcohol to glycolic acid at an industry-level current density over a Pd-Ni$(OH)_2$ catalyst, *Angewandte Chemie International Edition*, 2023, **62**, e202300094, doi: 10.1002/anie.202300094.

[7] L. Y. Zhang, J. J. Zhang, H. G. Yu, J. G. Yu, Emerging S-scheme photocatalyst, *Advance Materials*, 2022, **34**, 2107668, doi: 10.1002/adma.202107668.

[8] P. Zhou, I. A. Navid, Y. J. Ma, Y. X. Xiao, P. Wang, Z. W. Ye, B. W. Zhou, K. Sun, Z. T. Mi, Solar-to-hydrogen efficiency of more than 9% in photocatalytic water splitting, *Nature*, 2023, **613**, 66-70, doi: 10.1038/s41586-022-05399-1.

[9] E. Gong, S. Ali, C. B. Hiragond, H. S. Kim, N. S. Powar, D. Y. Kim, H. Kim, S. In, Solar fuels: research and development strategies to accelerate photocatalytic CO_2 conversion into hydrocarbon fuels, *Energy & Environmental Science*, 2022, **15**, 880-937, doi: 10.1039/d1ee02714j.

[10] X. Y. Tan, S. H. Si, D. F. Xiao, X. L. Bao, K. P. Song, Z. Y. Wang, Y. Y. Liu, Z. K. Zheng, P. Wang, Y. Dai, B. B. Huang, H. F. Cheng, Single cobalt atoms induced molecular O_2 activation for enhanced photocatalytic biomass upgrading on $ZnIn_2S_4$ nanosheets, *ACS Catalysis*, 2023, **13**, 14395-14403, doi: 10.1021/acscatal.3c03332.

[11] Q. G. Hao, Z. H. Li, Y. Q. Shi, R. Z. Li, Y. Li, L. Wang, H. Yuan, S. X. Ouyang, T. R. Zhang, Plasmon-induced radical-radical heterocoupling boosts photodriven oxidative esterification of benzyl alcohol over nitrogen-doped carbon-encapsulated cobalt nanoparticles, *Angewandte Chemie International Edition*, 2023, **62**, e202312808, doi: 10.1002/anie.202312808.

[12] J. J. Qin, J. H. Li, K. B. Chu, G. Z. Yang, L. Q. Zhang, X. M. Xia, P. Y. Xuan, X. Chen, B. Weng, H. W. Huang, Y. J. Chen, W. Fan, Y. B. Zhu, H. A. Wu, F. L. Lai, T. X. Liu, Biomimetic solar photocatalytic reactor for selective oxidation of aromatic alcohols with enhanced solar-energy utilization, *Advance Functional Materials*, 2024, **34**, 2311214, doi: 10.1002/adfm.202311214.

[13] C. S. Xian, J. He, Y. R. He, J. H. Nie, Z. L. Yuan, J. Sun, W. N. Martens, J. Z. Qin, H. Y. Zhu, Z. H. Zhang, High nitrile yields of aerobic ammoxidation of alcohols achieved by generating $^{\bullet}O_2^{-}$ and $Br^{\bullet}$ radicals over iron-modified TiO_2 photocatalysts, *Journal of the American Chemical Society*, 2022, **144**, 23321-23331, doi: 10.1021/jacs.2c07061.

[14] R. L. Pan, X. Ge, Q. Liu, H. Yin, Y. L. Guo, J. C. Shen, D. Y. Zhang, P. Chen, J. L. Yuan, H. B. Xie, C. B. Liu, Synergic delocalized-conjugate and electron-deficient effect and mesoporous channel promote photocatalytic coupling H_2 evolution with benzyl-alcohol oxidation, *Advance Functional Materials*, 2024, **34**, 2315212, doi: 10.1002/adfm.202315212.

[15] X. L. Xiang, B. C. Zhu, J. J. Zhang, C. H. Jiang, T. Chen, H. G. Yu, J. G. Yu, L. X.Wang, Photocatalytic H_2-production and benzyl-alcohol-oxidation mechanism over CdS using Co^{2+} as hole cocatalyst, *Applied Catalysis B: Environmental*, 2023, **324**, 122301, doi: 10.1016/j.apcatb.2022.122301.

[16] K. Sun, Y. Y. Qian, H. L. Jiang, Metal-organic frameworks

for photocatalytic water splitting and CO_2 reduction, *Angewandte Chemie International Edition*, 2023, **62**, e202217565, doi: 10.1002/anie.202217565.

[17] R. J. Yang, Y. Y. Fan, Y. F. Zhang, L. Mei, R. S. Zhu, J. Q. Qin, J. G. Hu, Z. X. Chen, Y. H. Ng, D. Voiry, S. Li, Q. Y. Lu, Q. Wang, J. C. Yu, Z. Y. Zen, 2D transition metal dichalcogenides for photocatalysis, *Angewandte Chemie International Edition*, 2023, **62**, e202218016, doi: 10.1002/anie.202218016.

[18] C. L. Tan , M. Y. Qi , Z. R. Tang, Y. J. Xu, Cocatalyst decorated $ZnIn_2S_4$ composites for cooperative alcohol conversion and H_2 evolution, *Applied Catalysis B: Environmental*, 2021, **298**, 120541, doi: 10.1016/j.apcatb.2021.120541.

[19] F. S. Xing, R. Y. Zeng, C. C. Cheng, Q. W. Liu, C. J. Huang, POM-incorporated $ZnIn_2S_4$ Z-scheme dual-functional photocatalysts for cooperative benzyl alcohol oxidation and H_2 evolution in aqueous solution, *Applied Catalysis B: Environmental*, 2022, **306**, 121087, doi: 10.1016/j.apcatb.2022.121087.

[20] P. Zhang, P. Y. Guo, M. S. Zhang, X. Y. Qiao, R. W. Wang, Z. T. Zhang, S. L. Qiu, Full-spectrum responsive dual-defect mediated S-scheme heterojunction for cooperative benzyl alcohol conversion and H_2 evolution, *Chemical Engineering Journal*, 2024, **479**, 147265, doi: 10.1016/j.cej.2023.147265.

[21] X. H. Wang, X. H. Wang, J. F. Huang, S. X. Li, A. Meng, Z. J. Li, Interfacial chemical bond and internal electric field modulated Z-scheme S_v-$ZnIn_2S_4$/$MoSe_2$ photocatalyst for efficient hydrogen evolution, *Nature Communications*, 2021, **12**, 4112, doi: 10.1038/s41467-021-24511-z.

[22] W. K. Chong, B. J. Ng, L. L. Tan, S. P. Chai, A compendium of all-in-one solar-driven water splitting using $ZnIn_2S_4$-based photocatalysts: guiding the path from the past to the limitless future, *Chemical Society Reviews*, 2024, **53**, 10080, doi: 10.1039/d3cs01040f.

[23] M. H. Xu, X. W. Ruan, D. P. Meng, G. Z. Fang, D. X. Jiao, S. L. Zhao, Z. Y. Liu, Z. F. Jiang, K. K. Ba, T. F. Xie, W. Zhang, J. Leng, S. Y. Jin, S. K. Ravi, X. Q. Cui, Modulation of sulfur vacancies in $ZnIn_2S_4$/MXene schottky heterojunction photocatalyst promotes hydrogen evolution, *Advance Functional Materials*, 2024, **34**, 2402330, doi: 10.1002/adfm.202402330.

[24] D. P. Kumar, K. H. Do, A. P. Rangappa, J. Lee, J. M. Wang, R. Boppella, M. Gopannagari, K. A. J. Reddy, D. A. Reddy, T. K. Kim, Highly stable and durable $ZnIn_2S_4$ nanosheets wrapped oxygen deficient blue TiO_2(B) catalyst for selective CO_2 photoreduction into CO and CH_4, *Journal of Colloid And Interface Science*, 2023, **651**, 264-272, doi: 10.1016/j.jcis.2023.07.197.

[25] M. Y. Qi, Q. Lin, Z. R. Tang, Y. J. Xu, Photoredox coupling of benzyl alcohol oxidation with CO_2 reduction over CdS/TiO_2 heterostructure under visible light irradiation, *Applied Catalysis B: Environmental*, 2022, **307**, 121158, doi: 10.1016/j.apcatb.2022.121158.

[26] B. Xing, T. Wang, Z. Q. Zheng, S. J. Liu, J. J. Mao, C. Li, B. X. Li, Synchronous fabrication of Ru single atoms and RuO_2 on hierarchical TiO_2 spheres for enhanced photocatalytic coproduction of H_2 and benzaldehyde, *Chemical Engineering Journal*, 2023, **46**, 141871, doi: 10.1016/j.cej.2023.141871.

[27] A. VahidMohammadi, J. Rosen, Y. Gogotsi, The world of two-dimensional carbides and nitrides (MXenes), *Science*, 2021, **372**, 1165, doi: 10.1126/science.abf1581.

[28] C. Cui, X. L. Zhao, X. W. Su, N. Xi, X. N. Wang, X. W. Yu, X. L. Zhang, H. Liu, Y. H. Sang, Porphyrin-based donor-acceptor covalent organic polymer/$ZnIn_2S_4$ Z-scheme heterostructure for efficient photocatalytic hydrogen evolution, *Advance Functional Materials*, 2022, **32**, 2208962, doi: 10.1002/adfm.202208962.

[29] C. F. Gong, H. Wang, J. Zhang, C. G. Yang, X. N. Bu, H. Y. Yang, J. Li, P. Gao, Construction of Active Rh-TiO_x Interfacial Sites on $RhFeO_x$/P25 for Highly Efficient Hydrogenation of CO_2 to Ethanol, *ACS Catalysis*, 2024, **14**, 17582-17597, doi: 10.1021/acscatal.4c04954.

[30] J. X. Bai, W. L. Chen, L. Hao, R. C. Shen, P. Zhang, N. Li , X. Li, Assembling Ti_3C_2 MXene into $ZnIn_2S_4$-$NiSe_2$ S-scheme heterojunction with multiple charge transfer channels for accelerated photocatalytic H_2 generation, *Chemical Engineering Journal*, 2022, **447**, 137488, doi: 10.1016/j.cej.2022.137488.

[31] G. Murali, J. K. R. Modigunta, Y. H. Park, J. H. Lee, J. S. Rawal, S. Y. Lee, I. In, S. J. Park, A review on mxene synthesis, stability, and photocatalytic applications, *ACS Nano*, 2022, **16**, 13370-13429, doi: 10.1021/acsnano.2c04750.

[32] Q. J. Tang, T. H. Li, W. G. Tu, H. Q. Wang, Y. Zhou, Z. G. Zou, Recent advances in diverse mxenes-based structures for photocatalytic CO_2 reduction into renewable hydrocarbon fuels, *Advance Functional Materials*, 2024, **34**, 2311609, doi: 10.1002/adfm.202311609.

[33] Y. G. Chao, P. Zhou, J. P. Lai, W. Y. Zhang, H. W. Yang, S. Y. Lu, H. Chen, K. Yin, M. G. Li, L. Tao, C. S. Shang, M. P. Tong, S. J. Guo, $Ni_{1-x}Co_xSe_2$-C/$ZnIn_2S_4$ hybrid nanocages with strong 2D/2D hetero-interface interaction enable efficient H_2-releasing photocatalysis, *Advance Functional Materials*, 2021, **31**, 2100923, doi: 10.1002/adfm.202100923.

[34] C. L. Jiang, H. Wang, Y. Q. Wang, H. B. Ji, All solid-state Z-scheme CeO_2/$ZnIn_2S_4$ hybrid for the photocatalytic selective oxidation of aromatic alcohols coupled with hydrogen evolution, *Applied Catalysis B: Environmental*, 2020, **277**, 119235, doi: 10.1016/j.apcatb.2020.119235.

[35] J. D. Hu, D. Y. Chen, Z. Mo, N. J. Li, Q. F. Xu, H. Li, J. H. He, H. Xu, J. M. Lu, Z-Scheme 2D/2D Heterojunction of Black Phosphorus/Monolayer Bi_2WO_6 Nanosheets with Enhanced Photocatalytic Activities, *Angewandte Chemie International*

Edition, 2019, **58**, 2073-2077, doi: 10.1002/ange.201813417.

[36] G. Z. S. Ling, S. H. W. Kok, P. P. Zhang, T. J. Siang, C. Y. Haw, L. L. Tan, B. H. Chen, W. J. Ong, All-in-one ultrathin nanoporous $ZnIn_2S_4$ with ameliorated photoredox capability: harvesting electron–hole pairs in cooperative hydrogen and benzaldehyde production, *Journal of Materials Chemistry A*, 2024, **12**, 1453-1464, doi: 10.1039/d3ta04204a.

Open Access